



# Enhanced activity of visible-light photocatalytic H<sub>2</sub> evolution of sulfur-doped g-C<sub>3</sub>N<sub>4</sub> photocatalyst via nanoparticle metal Ni as cocatalyst

Chuanzhi Sun<sup>a,b,\*</sup>, Hui Zhang<sup>a</sup>, Hao Liu<sup>a</sup>, Xiaoxue Zheng<sup>a</sup>, Weixin Zou<sup>b</sup>, Lin Dong<sup>b,\*</sup>, Lei Qi<sup>c</sup>

<sup>a</sup> College of Chemistry, Chemical Engineering and Materials Science, Collaborative Innovation Center of Functionalized Probes for Chemical Imaging in Universities of Shandong, Shandong Provincial Key Laboratory of Clean Production of Fine Chemicals, Institute of Materials and Clean Energy, Shandong Normal University, Jinan 250014, PR China

<sup>b</sup> School of the Environment, Jiangsu Key Laboratory of Vehicle Emissions Control, Center of Modern Analysis, Nanjing University, Nanjing 210093, PR China

<sup>c</sup> School of Chemistry and Chemical Engineering, University of Jinan, Jinan 250022, PR China

## ARTICLE INFO

### Keywords:

Sulfur doped graphitic carbon nitride  
Ni/g-S-C<sub>3</sub>N<sub>4</sub> photocatalytic hydrogen evolution  
H<sup>•</sup> Radical

## ABSTRACT

Sulfur doped graphitic carbon nitride g-S-C<sub>3</sub>N<sub>4</sub> (denoted as SCN) was successfully prepared, and the SCN was further combined with metal Ni to prepare the photocatalyst with high visible-light photocatalytic activity. The Ni/g-S-C<sub>3</sub>N<sub>4</sub> (denoted as NiSCN) composite photocatalyst was obtained by photodeposition method. Metal Ni species with the particle size about 5 nm were effectively supported on the surface of SCN. The NiSCN photocatalyst with the optimal Ni loading amounts exhibited an excellent H<sub>2</sub>-production rate of 2021.3 μmol g<sup>-1</sup> h<sup>-1</sup> under the visible light (λ > 420 nm). In addition, some Ni atoms might be embedded in the lattice structure of SCN. According to the experimental and computational results, the good utilization of visible light was attributed to the S and Ni doping, which upshifted the VB potential and narrowed the band gap of the photocatalyst. The metal Ni loaded on SCN surface improved the electron transfer rate and charge separation efficiency of the photocatalyst. Then, the H<sup>+</sup> in water obtained the electrons on metal Ni to form H<sub>2</sub> via the H<sup>•</sup> radical intermediate.

## 1. Introduction

With the rapid development of economy and modern industry, the environmental pollution and energy crisis have been the most challengeable and urgent problems to be solved [1,2]. Accordingly, development of small pollution and renewable energy has been a popular goal of scientists. Hydrogen is thought to be one of the promising candidates to solve the energy crisis as an environmentally friendly and renewable energy [3]. It is widely recognized that water is the most rich resources of hydrogen, and photocatalytic decomposition of water for hydrogen evolution is a broad development and sustainable methods [4,5]. Over the past decades, researchers have reported a variety of photocatalysts for hydrogen evolution from water [6,7]. However, although great progress and efforts have been made, there are still several challenges, such as low quantum efficiency in the visible light region and demanding for rare and expensive materials. Due to nearly 50% solar energy distributing in the visible light region, developing novel efficient visible-light-driven photocatalyst without noble metal are desirable [8].

Graphitic carbon nitride (g-C<sub>3</sub>N<sub>4</sub>, denoted as CN) polymer, a new

type of visible light photocatalyst, has attracted extreme attention and been widely studied owing to the excellent optical, thermal and electrical characteristics and low cost [9–11]. Unfortunately, the photocatalytic efficiency of pure CN is limited by its insufficient light-absorbance, slow charge mobility, and fast recombination rate of photogenerated electron-hole pairs [12]. In order to overcome these deficiencies, several modification strategies have been proposed in recent years, for instance, doping metal or nonmetal [13,14], fabricating heterojunctions with other semiconductors and so on [15–18]. Among them, doping nonmetal elements (e.g., sulfur) to CN via high-temperature thermal polymerization method is a convenient method to prepare high efficiency photocatalyst [19]. The sulfur doped CN exhibits better visible-light-responsive property than that of CN due to the narrowed band gap and the excellent efficiency of charge transfer [20]. Thus, the S doped CN is a promising photocatalyst for hydrogen evolution from water under visible light.

The immobilization of cocatalyst onto the surface of CN is one of the effective strategies for improving the photocatalytic hydrogen evolution, which can improve the separation of photogenerated electron-hole pairs [21]. Noble metals such as platinum (Pt) [22], gold (Au) [23],

\* Corresponding authors at: School of the Environment, Jiangsu Key Laboratory of Vehicle Emissions Control, Center of Modern Analysis, Nanjing University, Nanjing 210093, PR China

E-mail addresses: [suncz@sdu.edu.cn](mailto:suncz@sdu.edu.cn) (C. Sun), [donglin@nju.edu.cn](mailto:donglin@nju.edu.cn) (L. Dong).

<https://doi.org/10.1016/j.apcatb.2018.04.050>

Received 17 December 2017; Received in revised form 12 April 2018; Accepted 21 April 2018

Available online 22 April 2018

0926-3373/ © 2018 Elsevier B.V. All rights reserved.

silver (Ag) [24] and palladium (Pd) [25] are usually the most common cocatalysts for improving the photocatalytic performance of CN. However, noble metal is rare and expensive, and it is necessary to develop new, low-cost and earth-abundant cocatalysts for replacing noble metal. In the non-noble metals, nickel-based catalysts have attracted widely attention in photocatalytic hydrogen production, such as, Ni(OH)<sub>2</sub> [26], NiS [27], Ni(dmgH)<sub>2</sub> complex [28], Ni<sub>2</sub>P [29], Ni(triethanolamine)<sub>2</sub>Cl<sub>2</sub> complex [30] etc. Particularly, metal Ni can play the similar role to the noble metals and take an important effect on improving the separation efficiency of electron-hole pairs [31].

In this work, sulfur was introduced to CN for improving the utilization of visible light and Ni(O) was employed as cocatalyst. Ni(O) was generated from the reduction of Ni(II) by photogenerated electrons of SCN [31]. The optimal NiSCN catalyst exhibited a high H<sub>2</sub> production rate of 2021.3 μmol h<sup>-1</sup> g<sup>-1</sup> under visible light (λ > 420 nm), which was 334.1 times higher than pure CN and 83.7 times higher than SCN catalyst. The location and doping effect of sulfur and nickel were studied by experimental and theoretical method, and the chemical states and effects of metal Ni were investigated. In addition, the photocatalytic mechanism of H<sub>2</sub> production was also discussed.

## 2. Experimental section

### 2.1. Photocatalysts preparation

The SCN photocatalyst was prepared by high-temperature thermal polymerization method, the specific preparation process is as follows: urea (10 g) and benzyl disulfide (1 g) were dispersed in ethanol with ultrasonic for 30 min, and stirred for 1 h at room temperature to make it completely dispersed. Then, the mixture was evaporated in an oil bath at 70 °C. After that, the mixture was placed in a crucible and calcined at 600 °C for 2 h with a heating rate of 3.5 °C min<sup>-1</sup> under N<sub>2</sub> flow. The resulting product was ground to powder finally. For comparison, a sample of CN prepared by direct calcinating urea (10 g) in the same conditions.

The NiSCN composite photocatalysts were synthesized by photo-deposition method. In detail, the prepared SCN samples (0.2 g) were dispersed in 200 ml aqueous solution containing 10 vol% triethanolamine (TEOA), a certain amount of 0.1 M nickel nitrate (Ni(NO<sub>3</sub>)<sub>2</sub>·6H<sub>2</sub>O) and 0.1 M sodium hypophosphite (NaH<sub>2</sub>PO<sub>2</sub>) solution in a quartz flask. Then, other residual gases of the mixed system were removed through the vacuum. This suspension was stirred and irradiated for 1 h under UV-vis light (300 W Xe lamp). After that, the product was filtered and washed with distilled water, and finally dried in a vacuum at 50 °C overnight. The amounts of deposited nickel can be adjusted by changing the concentration of Ni(NO<sub>3</sub>)<sub>2</sub> and NaH<sub>2</sub>PO<sub>2</sub> solution. The amounts of nickel species in solution are calculated relative to the amounts of SCN with 1 wt%, 3 wt%, 5 wt%, 8 wt%, 10 wt% and 15 wt%, which is denoted as NiSCN1, NiSCN3, NiSCN5, NiSCN8, NiSCN10, NiSCN15, respectively. For comparison, NiCN5 was also prepared using the same method.

### 2.2. Characterization

The X-ray diffraction (XRD) patterns were recorded on a Philips X'pert Pro diffractometer with Cu Kα radiation (λ = 0.15418 nm) at a scan rate of 5° min<sup>-1</sup>. The X-ray tube was operated at 40 kV and 40 mA. Transmission electron microscopy (TEM) and high-resolution transmission electron microscopy (HRTEM) images were obtained on JEM-2100 instrument at an acceleration voltage of 200 kV. The scanning transmission electron microscopy (STEM) images were collected using an FEI Tecnai F30 TEM operating at an accelerating voltage of 300 kV with high-angle annular dark-field (HAADF) detector. The Tecnai F30 was equipped with an energy-dispersive X-ray (EDX) spectrometer, which was utilized for the elemental mapping of selected areas. Inductively coupled plasma-optical emission spectrometry (ICP-OES)

was performed on Thermo Scientific iCAP 7000 apparatus to determine the actual concentrations of elements in samples. The Brunauer-Emmett-Teller (BET) surface areas were measured using a Micromeritics ASAP-2020 analyzer at 77 K. Approximate 100 mg of sample was degassed at 300 °C for 3 h in the N<sub>2</sub>/He mixture before each adsorption measurement. The X-ray photoelectron spectroscopy (XPS) measurements were conducted by a PHI 5000 Versa Probe X-ray photoelectron spectrometer with a monochromatic Al Kα (1486.6 eV) radiation source (15 kW). Prior to testing, samples were degassed to below 5 × 10<sup>-7</sup> Pa in an ultrahigh vacuum chamber at room temperature. The charge effect is compensated by correcting the C 1s spectrum to 284.6 eV, and the precision of the binding energy is ± 0.1 eV. Photoluminescence (PL) spectra were measured by an FLS-920 Edinburgh fluorescence spectrometer. The Fourier transform infrared (FTIR) spectra were recorded on a Nicolet iS50 FT-IR spectrometer. UV-vis absorbance spectra of samples in 200–800 nm region were obtained by UV-vis spectrophotometer (X-3, YuanXi Instruments). Electrochemical and photoelectrochemical experiments were performed on a CHI-660C electrochemical analyzer in a standard three-electrode system with a working electrode, and a Pt plate as the counter electrode and Ag/AgCl (saturated KCl) as a reference electrode. A Xe lamp (300 W) with a UV cut-off filter (λ > 420 nm) was used as light source. The 0.1 M Na<sub>2</sub>SO<sub>4</sub> was employed as electrolyte solution. The transient photocurrent response and the electrochemical impedance spectra (EIS) were measured at 0.5 V. The working electrode was prepared as follows: 2 mg sample were added into 2 ml ethanol solution containing 10 μL 0.25% Nafion to obtain a slurry. Then, the resulting product was dropped onto a fluorine-doped tin oxide (FTO) glass piece (1 cm × 2 cm) and dried in an oven at 100 °C for 10 h. Mott-Schottky (M-S) analysis was measured at polarization potential from -0.5 V to 1.5 V (vs. SCE), with an alternating current potential frequency of 1000 Hz. The Electron spin resonance (ESR) signals of radicals were recorded by a Bruker A300-10/12/S-LC spectrometer using 2-methyl-N-(4-pyridinylmethylene)-2-propanamine N,N'-dioxide (POBN) as a spin trap.

### 2.3. DFT calculations

The geometry optimizations were performed using the B3LYP density functional method in Gaussian 09. The standard 6-31G(d) basis set was used for H, C, N and S atoms. However, the effective core potentials of Hay and Wadt combined with double-ζ valence basis sets (LanL2DZ) were used for Ni. The molecular structural models of CN and SCN were built using a truncated structure comprising three melons, and two possibilities (N or C replaced by S) are all considered. The fringe C/N atoms were compensated by H to eliminate boundary influence.

### 2.4. Photocatalysis test

The photocatalytic hydrogen production system was performed in a quartz flask. Specific steps: 0.2 g sample were dispersed in an aqueous solution (200 ml) containing 20 vol% TEOA. This system was evacuated to remove the residual gas. Then, the photocatalytic system was irradiated with 300 W Xe arc lamp with an ultraviolet cutoff filter (λ > 420 nm) under magnetic stirring. The hydrogen production is analyzed by a gas chromatograph (GC-7900, TCD, Ar as the carrier gas, and 5 Å molecular sieve column.)

The external quantum efficiency (EQE) for H<sub>2</sub> evolution was measured by the Xe lamp with a set of band-pass filters (λ = 405 nm, 420 nm, 450 nm and 500 nm), the irradiation intensities were determined by a NOVA II laser power meter (Ophir Photonics). The EQE was calculated according to (1)

$$\text{EQE}(\%) = \frac{\text{number of reacted electrons}}{\text{number of incident photons}} \times 100\% \\ = \frac{\text{number of evolved H}_2 \text{ molecules} \times 2}{\text{number of incident photons}} \times 100\% \quad (1)$$

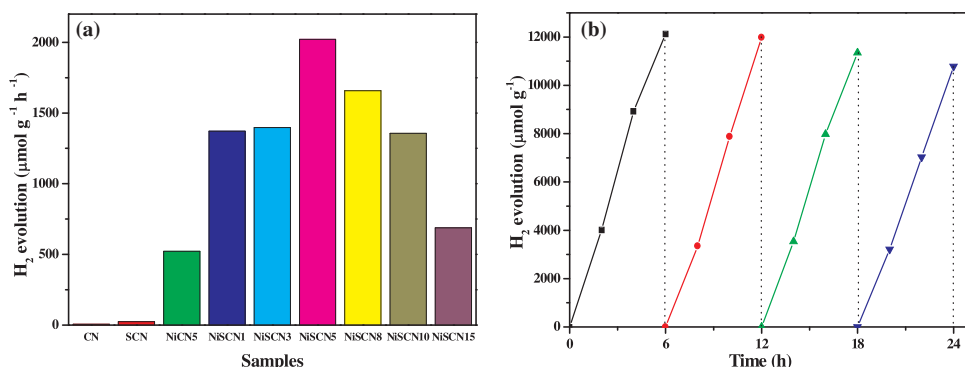


**Fig. 1.** (a) The photocatalytic H<sub>2</sub>-production activities of CN, SCN, NiCN5, NiSCN1, NiSCN3, NiSCN5, NiSCN8, NiSCN10 and NiSCN15 samples. (b) Photocatalytic H<sub>2</sub>-production of 24 h on NiSCN5 photocatalyst with evacuation every 6 h. Reaction conditions: 0.2 g photocatalyst, 160 mL H<sub>2</sub>O, 40 mL TEOA, 300 W Xe lamp equipped with a cut-off filter at 420 nm.

### 3. Results and discussion

#### 3.1. Photocatalytic hydrogen production activity of samples

Photocatalytic hydrogen production activities on different samples were measured under visible light irradiation ( $\lambda > 420$  nm) using TEOA as a hole scavenger reagent. In the present study, no significant hydrogen production was detected in the absence of either visible-light irradiation or photocatalyst, suggesting hydrogen was produced by photocatalytic reactions. Fig. 1(a) shows the photocatalytic H<sub>2</sub>-production activities of different samples. As can be seen, without any cocatalyst, the photocatalytic H<sub>2</sub>-production rate is almost negligible for pure CN because of the fast recombination between conduction band (CB) electrons and valence band (VB) holes [26]. The SCN photocatalyst exhibits a weak visible-light hydrogen production rate with about  $24.2 \mu\text{mol g}^{-1} \text{h}^{-1}$ , suggesting the S addition can increase the activity of CN. After a small amount of nickel is introduced, the activity of the SCN photocatalyst is significantly increased. The NiSCN5 photocatalyst exhibits the highest hydrogen production rate with  $2021.3 \mu\text{mol g}^{-1} \text{h}^{-1}$ . In addition, NiCN5 photocatalyst is prepared for comparison, but the activity of it is also much lower than that of the NiSCN5 photocatalyst, as shown in Fig. 1(a) ( $529.1 \mu\text{mol g}^{-1} \text{h}^{-1}$ ). The activity of NiSCN5 under visible-light is also compared with the systems based on  $\text{g-C}_3\text{N}_4$ , as displayed in Table S1. As can be seen, the NiSCN5 catalyst shows better activity than the other catalysts. Therefore, the S and Ni species play an important role in promoting the activities of photocatalysts. Furthermore, the photocatalytic activity decreases when excess amounts of Ni ( $> 5.0$  wt%) are introduced. Photocatalytic H<sub>2</sub>-production experiments were performed by time-cycles to test the stability of the NiSCN5 composite photocatalyst, as shown in Fig. 1(b). After four cycles, the H<sub>2</sub>-production rates decrease a little, which indicates the photocatalysts are relatively stable in the photocatalytic H<sub>2</sub>-production process. In addition, as displayed in Table S2, the external quantum efficiency (EQE) of NiSCN5 sample was tested to be 3.20%, 2.51%, 1.64% and 0.80% under the light with the wavelength of 405 nm, 420 nm, 450 nm and 500 nm, respectively. As can be seen, the NiSCN5 photocatalyst shows considerable quantum efficiency when the wavelength is higher than 450 nm.

#### 3.2. Morphology and composition of SCN and NiSCN samples

XRD measurements were performed to investigate the phase structure of the samples. Fig. 2(a) shows the XRD patterns of pure CN, SCN and NiSCN5 samples. It can be seen that pure CN exhibits two distinct diffraction peaks located at  $2\theta = 27.6^\circ$  and  $13.0^\circ$ , which is consistent with the results reported in literatures [9,32]. The strong diffraction peak at  $27.6^\circ$  represents interlayer stacking reflection of conjugated aromatic systems corresponding to the interlayer distance of 0.324 nm, and can be indexed to the (002) crystal plane [9]. The weak peak at  $13.0^\circ$  ascribed from (100) plane is related to an in-plane structural

packing motif corresponding to an interplanar separation of 0.680 nm [33]. Furthermore, for the SCN and NiSCN5 samples, no significant shift of the main peak at  $27.6^\circ$  can be observed, indicating the doping of sulfur and deposition of nickel did not change the crystal structure of CN. The XRD patterns of NiSCN with different loading amounts of Ni species are shown in Fig. 2(b). The intensity of diffraction peaks of SCN are unchanged firstly (Ni contents  $< 8.0$  wt%). Then it decreases with the content of Ni increasing, which should be attributed to more nickel species covering on the surface of SCN. In addition, it is noteworthy that no characteristic diffraction peaks of Ni can be observed in all NiSCN samples, suggesting Ni nanoparticles are very small and highly dispersed on the surface of SCN.

The nitrogen adsorption-desorption isotherms were used to investigate textural properties of the CN, SCN and NiSCN5 photocatalysts. Fig. 3 shows the isotherms and the corresponding pore-size distribution curves (the inset) of these samples. It clearly shows that all tested samples can be categorized as type IV isotherms with H3 hysteresis loops [34]. In addition, the nitrogen adsorption increases rapidly at  $p/p_0$  approaching 1.0, suggesting that a large number of mesopores may exist in these samples. The corresponding pore-size distribution curves (inset in Fig. 3) further confirm the distribution of the pore size is mainly from 2 to 10 nm. The specific surface area of CN is  $82.4 \text{ m}^2 \text{g}^{-1}$ , and the introduction of S makes little change of the surface area (SCN:  $85.1 \text{ m}^2 \text{g}^{-1}$ ). The NiSCN5 shows a significant decrease of surface area ( $60.41 \text{ m}^2 \text{g}^{-1}$ ), which should be due to the loading of Ni nanoparticles on the surface of SCN [35]. As can be seen, the surface area of NiSCN5 is the lowest among the three samples, however, the activity of it is the highest. These results suggest no direct relationship between surface areas and the activities of photocatalysts, and the improvement of the activity is mainly induced by changing the electronic structure after S and Ni introduction.

The microstructure and morphology of NiSCN5 composite was investigated by TEM and the high resolution TEM (HRTEM). As seen in Fig. 4(a), Ni nanoparticles are dispersed on the SCN surface. The HRTEM image shows the size of the particles is 4–7 nm and the distance between two adjacent lattice fringes of the nanoparticle is about 0.203 nm (Fig. 4(b)), which is consistent with the spacing of (111) plane of metal Ni [36]. The intimate interface contact between Ni and SCN benefits the charge transfer from SCN to Ni, which will facilitate electron-hole separation and improve photocatalytic efficiency. The STEM image and the corresponding EDX elemental mapping images of C, N, S and Ni are shown in Fig. 4(c). As can be seen, the S elements exist, and Ni species can also be detected in the NiSCN5 catalyst.

The chemical structures of the photocatalysts were analyzed by FTIR spectra, as shown in Fig. 5. Three strong absorption peaks at  $3100\text{--}3300 \text{ cm}^{-1}$ ,  $1200\text{--}1700 \text{ cm}^{-1}$  and  $812 \text{ cm}^{-1}$  present in all the samples. The broad peaks in the range  $3100\text{--}3300 \text{ cm}^{-1}$  are residual N–H components and O–H bonds, possibly due to the unpolymerized amino groups and surface adsorbed water molecules [37]. The peaks in the range of  $1200\text{--}1700 \text{ cm}^{-1}$  belongs to the typical stretching vibration of aromatic C–N heterocycles, which is consistent with the FTIR



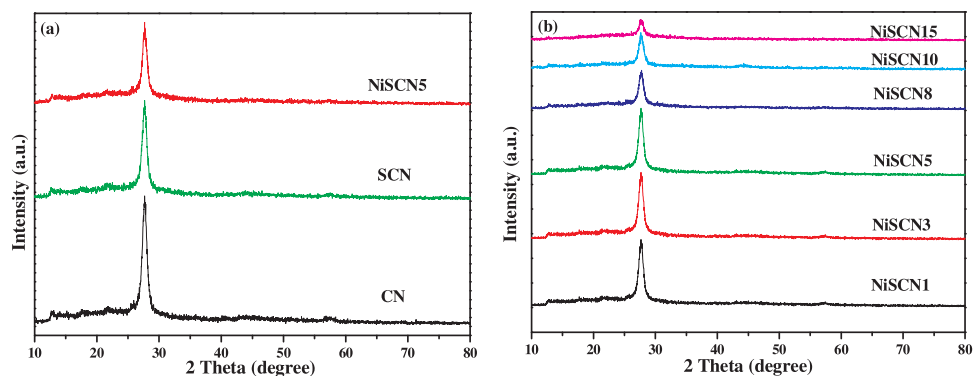


Fig. 2. XRD patterns of (a) CN, SCN and NiSCN5 samples; (b) NiSCN samples with different Ni contents.

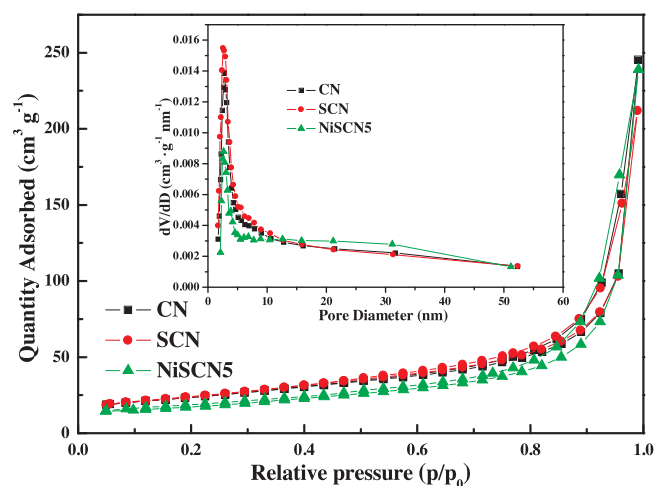


Fig. 3. Nitrogen adsorption-desorption isotherms and the corresponding pore size distribution curves (inset) of CN, SCN and NiSCN5 samples.

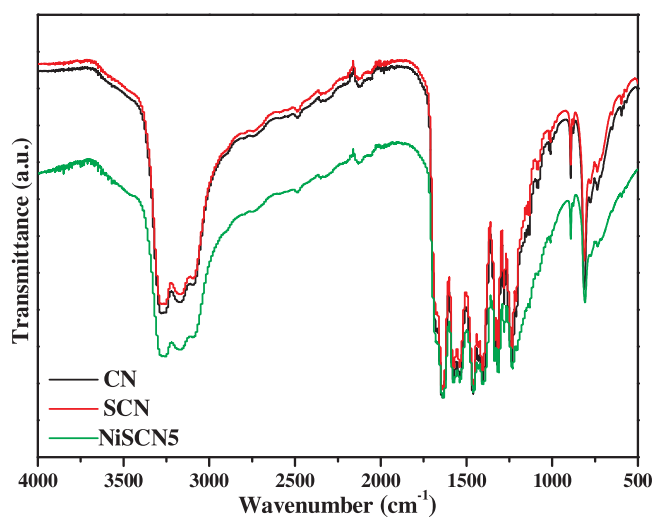


Fig. 5. IR spectra of CN, SCN and NiSCN5 samples.

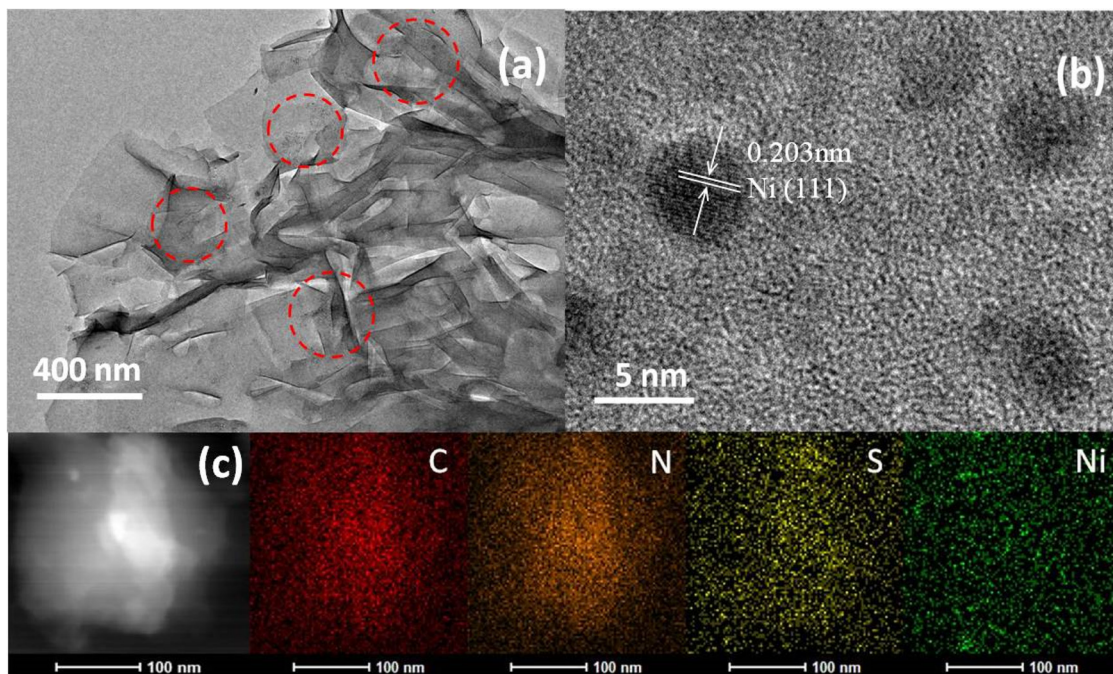


Fig. 4. (a) TEM image, (b) HRTEM image and (c) STEM and STEM-EDX elemental mapping of NiSCN5 sample.

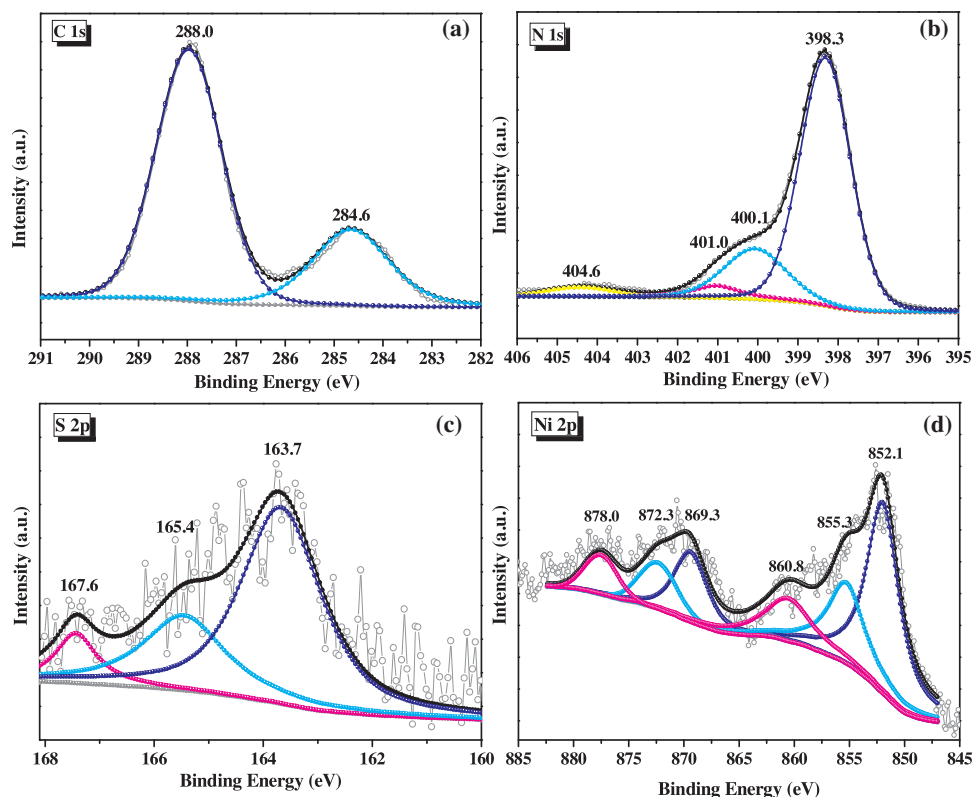


Fig. 6. XPS spectra of (a) C 1s, (b) N 1s, (c) S 2p and (d) Ni 2p of NiSCN5 sample.

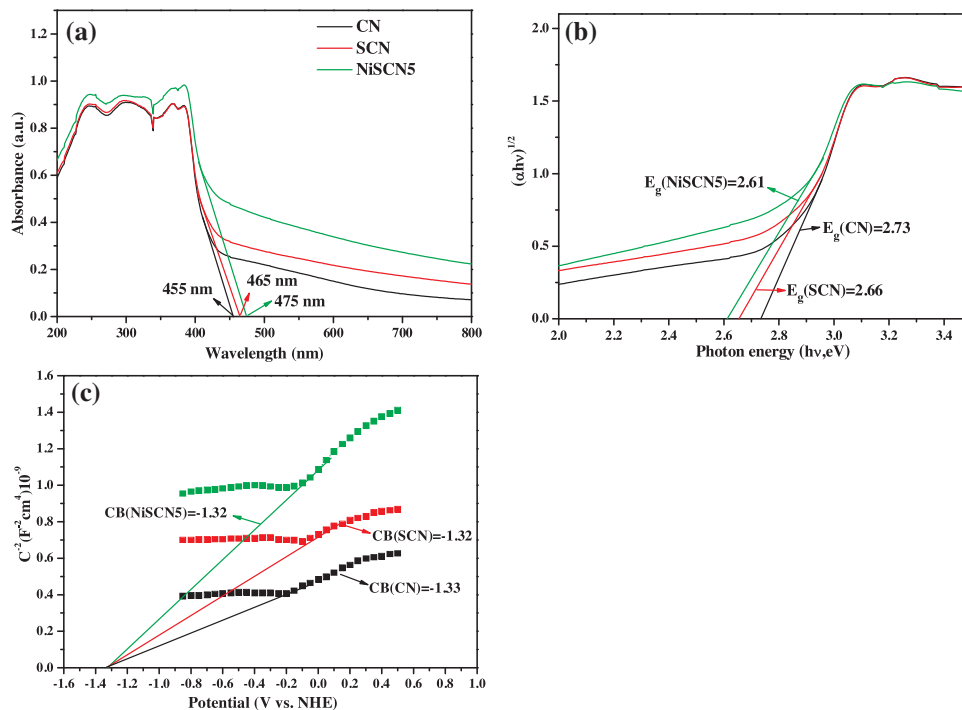


Fig. 7. (a) UV-vis diffuse reflectance spectra, (b) Plots of  $(\alpha h\nu)^{1/2}$  vs. photon energy ( $h\nu$ ) and (c) Electrochemical Mott-Schottky plots of CN, SCN and NiSCN5 samples.

analysis of CN reported in the literature [38]. Additionally, the stretching vibration of triazine ring units was observed at  $812\text{ cm}^{-1}$  [39]. The FTIR spectra of SCN and NiSCN5 samples are similar with CN sample, suggesting that the chemical structure of CN is not changed after S and Ni species introduction.

The composition and chemical states of elements for NiSCN5 sample

were analyzed by XPS, as shown in Fig. 6. Fig. 6(a) shows the C 1s spectra with two peaks at binding energies of 284.6 eV and 288.0 eV. The peak at 284.6 eV could be ascribed to the  $\text{sp}^2$  C–C bonds of carbon, which is from carbon conductive tape [40]. The other peak at 288.0 eV could be attributed to the  $\text{sp}^2$ -bonded carbon in the N-containing aromatic ring ( $\text{N}=\text{C}=\text{N}$ ) [41]. The N 1s spectrum is shown in Fig. 6(b),

and binding energies at about 398.3 eV, 400.1 eV, 401.0 eV and 404.6 eV can be observed. The main peak at 398.3 eV can be assigned to  $sp^2$ -hybridized nitrogen (C=N-C), and the three small peaks located at 400.1 eV, 401.0 eV and 404.6 eV originate from the N-C<sub>3</sub> groups, N-H and  $\pi$ -excitation, respectively [26,42,43]. The S 2p peak are shown in Fig. 6(c), which can be deconvoluted into three peaks at 163.7 eV, 165.4 eV and 167.6 eV, respectively. The strong peak at 163.7 eV represents the C-S bond, and the weak peak at 165.4 eV is ascribed to the N-S bond. The weak peak at 167.6 eV suggests some oxidized S (SO<sub>x</sub>) species also exist [44–47]. The binding energies of 160–164 eV region are attributed to the formation of  $S^{2-}$  species, whereas the XPS peaks in the range of 167–170 eV are due to the presence of  $S^{4+}$ ,  $S^{6+}$  species [46,48,49]. Accordingly, both N and C may be replaced by S in g-C<sub>3</sub>N<sub>4</sub> lattice. Fig. 6(d) shows the XPS spectrum of Ni 2p. The strongest peak at 852.1 eV (Ni<sup>0</sup> 2p<sub>3/2</sub>), together with the peak at 869.3 eV (Ni<sup>0</sup> 2p<sub>1/2</sub>), corresponds to the metallic Ni. The binding energy at 855.3 eV is attributed to the Ni<sup>2+</sup> 2p<sub>3/2</sub> peak, and 872.3 eV is assigned to the Ni<sup>2+</sup> 2p<sub>1/2</sub> peak. The emergence of Ni<sup>2+</sup> is attributed to the oxidation of metallic nickel by O<sub>2</sub> when the NiSCN5 sample exposes in the air. In addition, the satellite signal at 860.8 eV for Ni<sup>2+</sup> 2p<sub>3/2</sub> and 878.0 eV for Ni<sup>2+</sup> 2p<sub>1/2</sub> can be detected [50–52]. The amount of S-doping of the SCN catalyst is analyzed by Elemental Analyzer, and the atomic composition of C, N, and S of SCN were 39.81%, 60.14% and 0.05%, respectively. The C:N ratio for SCN (0.66) was lower than CN (0.75), which may be attributed to the partial residual precursors of urea (the ratio of C:N is 0.5) also existing in the sample [53].

### 3.3. Optical and electrochemical properties of CN, SCN and NiSCN5 samples

The UV–vis spectra were used to study the optical properties of pure CN, SCN and NiSCN5 and shown in Fig. 7(a). As shown in Fig. 7(a), the absorption edge of pure CN is around 455 nm corresponding to a band of 2.73 eV. When S was doped, the absorption edge is changed to about 465 nm indicating a red shift is induced by the S doping into the lattice of CN. The absorption edge shifts to 475 nm for the NiSCN5 photocatalyst. The result indicates that, except nanoparticle metal Ni loading on the surface of SCN, some Ni atoms may be embedded in the lattice structure of SCN leading to the red shift of the absorption edge. Therefore, the visible-light response of NiSCN5 catalyst is significantly improved. In order to prove the existence of Ni doping, the surface metallic Ni species of NiSCN5 sample were removed by the 5 M HNO<sub>3</sub>, and the acid treated sample is denoted as NiSCN5-A. Through comparing the ICP results of NiSCN5 and NiSCN5-A samples (shown in Table S3), it can be seen that most of Ni species were removed by HNO<sub>3</sub> and only 0.01 wt% Ni species left in the NiSCN5-A sample. The UV–vis diffuse reflectance spectrum of NiSCN5-A sample is displayed in Fig. S1 to compare with that of the NiSCN5 and SCN samples. As can be seen, the UV–vis spectra of NiSCN5 and NiSCN5-A samples almost overlap each other. The results suggest large amounts of metallic Ni species on the surface of SCN take no effect on the absorption edge, while the Ni atoms embedded in the lattice structure of SCN make the red shift of the absorption edge. Fig. 7(b) shows the Kubelka-Munk function vs. the energy of the absorbed light. As can be seen, the eigen band-gap energy decreases from 2.73 (CN) to 2.66 (SCN) and 2.61 (NiSCN5). Fig. 7(c) gives the Mott-Schottky plots of CN, SCN and NiSCN5 samples. According to intercept value in Fig. 7(c), the conduction band (CB) potential was approximate -1.33, -1.32, and -1.32 (vs. NHE) for CN, SCN, and NiSCN5, respectively. Consequently, the valence band (VB) potential of different samples were calculated to be 1.4 V (CN), 1.34 V (SCN) and 1.29 V (NiSCN5) vs. NHE. The results suggest the CB potentials of the photocatalysts change little and the VB potentials show an upshift, and the doping of S and Ni narrows the band gap of the photocatalysts.

In order to further investigate the doping effect of S and Ni on the electronic structure of SCN and NiSCN5, DFT calculations were

performed and the structure model of CN, SCN and NiSCN constituting with melon units are shown in Fig. 8. The structure model shows the S may substitute C or N site forming C-substituted or N-substituted SCN (Fig. 8(b) and (d)) and NiSCN (Fig. 8(c) and (e)). The difference between the highest occupied molecular orbital (HOMO) and the lowest unoccupied molecular orbital (LUMO) was calculated. The calculated results suggest that the values of LUMO are almost unchanged, and the HOMO shows upward shift after the C or N is substituted by S. When the Ni embeds into the central hollow site of SCN, the HOMO shows further upward shift. These results suggest doping of Ni atom to SCN lattice seems reasonable, which is also in agreement with the experimental results. The band gaps between HOMO and LUMO are calculated to be 0.14 a.u. (CN), 0.08 a.u. (C-substituted SCN), 0.04 a.u. (C-substituted NiSCN), 0.05 a.u. (N-substituted SCN) and 0.03 a.u. (N-substituted NiSCN). The results indicate the band gap will be narrowed after S and Ni introduction, which is also accordance with the experimental results. The molecular orbitals of SCN were analyzed by DFT calculation and shown in Fig. S2. The results suggest the HOMO mainly populated around the S atom and the atoms near S, while the LUMO mainly populated in the other atoms of SCN. The results suggest the S2p orbitals make main contribution to HOMO, which maybe the reason for the upward shift of VB potentials. In addition, the molecular orbitals show that Ni can be fixed in the hollow site through the interaction of Ni3d and N2p/S2p orbitals, as shown in Fig. S3.

The photoluminescence (PL) analysis was performed to study the synergetic effect of S and Ni on charge carrier separation. Fig. 9 presents the PL spectra of CN, SCN and NiSCN5 with an excitation wavelength of 325 nm. As seen in Fig. 9, it is evident that these samples show similar emission trends, but the peak intensities are different. The SCN has the lower PL intensity than CN, and the NiSCN5 sample displays the lowest PL intensity. The results suggest doping of S to CN decline radiative recombination, indicating S doping can promote the electron transfer rates [20]. The deposition of Ni on the surface of SCN further effectively inhibits the recombination of photogenerated electron-hole pairs. Combined the photocatalytic activity of NiSCN5, it can be concluded that loading of metal Ni on the surface of photocatalyst is more important for the separation of electron-hole pairs.

The electrochemical properties were measured to investigate the photogenerated charge separation and electron transfer process. Photocurrent responses of CN, SCN and NiSCN5 are shown in Fig. 10(a). The transient photocurrent response of a photocatalyst may be directly related to the recombination efficiency of photogenerated electron [54]. It can be seen that the doping of S to CN is helpful for the enhancement of photocurrent response. Compared with CN and SCN, the NiSCN5 sample shows the best photocurrent response, which is about 4.0 times higher than that of CN. The result reveals that the photoinduced electrons and holes in the NiSCN5 sample were separated more efficiently than that in the SCN and CN sample, which should be attributed to the conduction role of metal Ni nanoparticles. The electrochemical impedance spectra (EIS) were also carried out to evaluate the separation efficiency of photogenerated charge of the photocatalysts, as shown in Fig. 10(b). The Nyquist curve radius reflects the surface reaction speed and the size of electrode resistance for photocatalyst [55]. The semicircles of the Nyquist plots corresponding to the SCN are reduced compared with CN, suggesting S doping into CN obviously improves the rate of charge transfer. NiSCN5 displays the shortest semicircle among the three samples, which reveals that the loading of metal Ni on SCN surface further accelerates electron transfer process [56]. To evaluate the photoelectric conversion efficiency, the IPCE plots of the samples were recorded at a bias of 0.5 V. The results were calculated according to the equation [57]:

$$\text{IPCE (\%)} = (1240I) / (\lambda J_{\text{light}})$$

Where  $I$  is the measured photocurrent density ( $\text{mA cm}^{-2}$ ),  $\lambda$  is the wavelength of incident light (nm),  $J$  is the measured irradiance

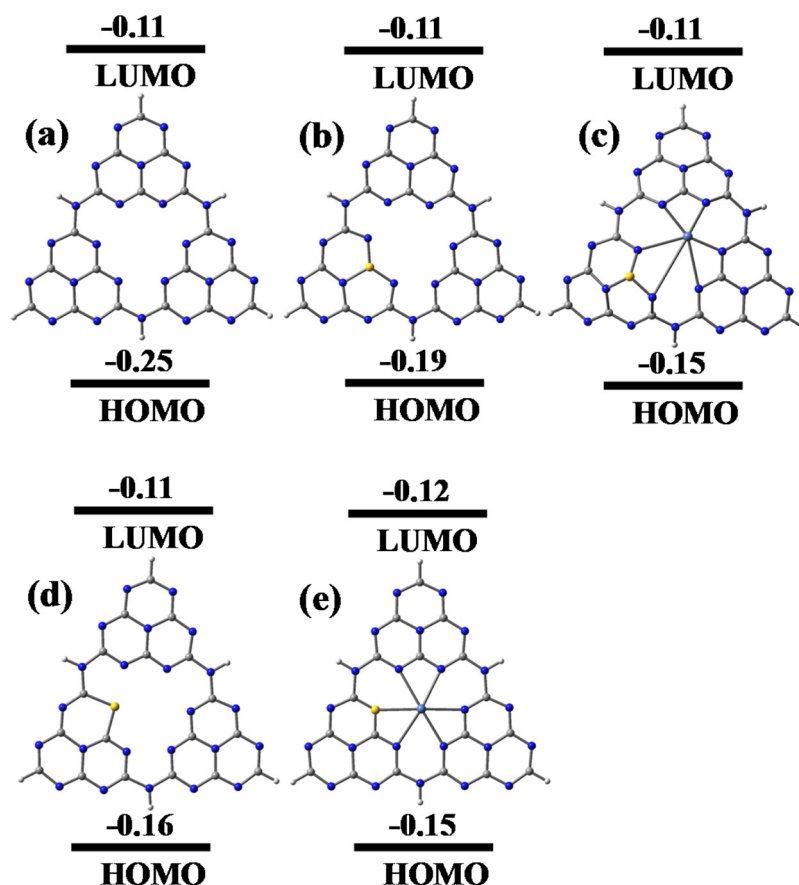


Fig. 8. Structure model of (a) CN, (b) SCN (C-substituted), (c) NiSCN (C-substituted), (d) SCN (N-substituted) and (e) NiSCN (N-substituted) Gray: C, blue: N, light blue: Ni and Yellow: S (For interpretation of the references to colour in this figure legend, the reader is referred to the web version of this article).

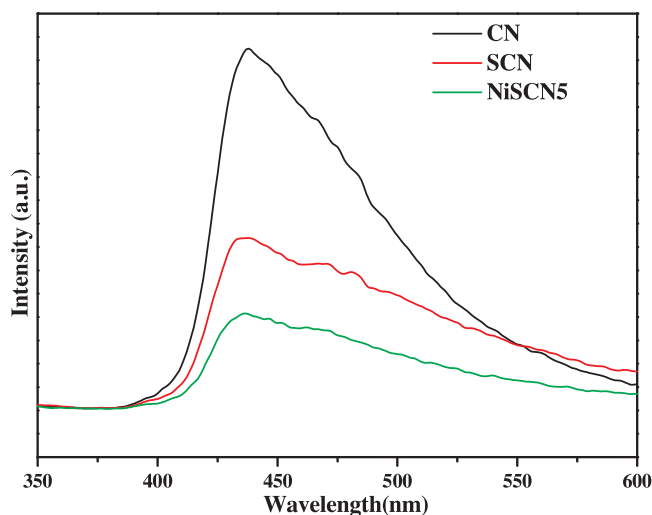


Fig. 9. Photoluminescence spectra of CN, SCN and NiSCN5 samples.

intensity ( $\text{mW}\cdot\text{cm}^{-2}$ ). As shown in Fig. 10(c), the shapes of the IPCE curves for all samples are similar, and the IPCE values decreased with increasing wavelength from 360 to 600 nm. The IPCE of the NiSCN5 electrodes is 12.26% at 400 nm, which shows about 3.45 and 2.21 times compared with CN and SCN at the same wavelength, respectively. The order of the IPCE of the three samples is consistent with photocurrent and EIS measurements. In addition, the IPCE of NiSCN5 in the longer wavelength (from 400 to 600 nm) also is higher than that of SCN, and the CN shows the lowest IPCE. Therefore, the loading of Ni on SCN surface effectively suppresses the recombination of electron-hole pairs,

and improves the separation and immigration of charge and the photoelectric conversion efficiency.

#### 3.4. Photocatalytic mechanism of $\text{H}_2$ production

ESR measurements were performed to monitor free radicals during the reaction process. Fig. 11 shows the POBN spin-trapping ESR spectra of CN, SCN and NiSCN5. The POBN- $\text{H}\cdot$  adduct, as reported in literature, can be observed in the three photocatalytic systems under visible light irradiation [58]. The results suggest that the  $\text{H}\cdot$  radical is an intermediate for the photocatalytic  $\text{H}_2$  evolution from water over the g- $\text{C}_3\text{N}_4$  based catalysts. However, the formation rates of  $\text{H}\cdot$  radical over the three photocatalysts are different. As seen in Fig. 11, at the 5th minute, the peaks can be hardly observed in the CN photocatalytic system. However, the peak intensities are stronger in the SCN system, and NiSCN5 photocatalytic system shows the strongest peak intensities. Furthermore, the peak intensities of the three systems follow the order of  $\text{CN} < \text{SCN} < \text{NiSCN5}$ . These results suggest that S doping and Ni loading promote the  $\text{H}\cdot$  radical formation and improve the  $\text{H}_2$  evolution.

On the basis of the above results, a possible mechanism for visible-light excitation and separation of electron-hole pairs at the interface between nickel nanoparticle and sulfur doped CN photocatalyst is proposed in Scheme 1. Normally, it is suggested that electrons ( $\text{e}^-$ ) are excited from the VB to the CB of CN, creating holes ( $\text{h}^+$ ) in the VB [33]. Doping of S to CN makes VB potential show an upward shift, and doping of Ni to SCN further upshifts the VB potential. Thus, much more visible light can be utilized for the NiSCN catalysts. Moreover, surface metal Ni takes an important effect on the separation efficiency of photogenerated electron-hole pairs. When SCN is connected with metal Ni forming interface, the photogenerated electrons in the CB of SCN will



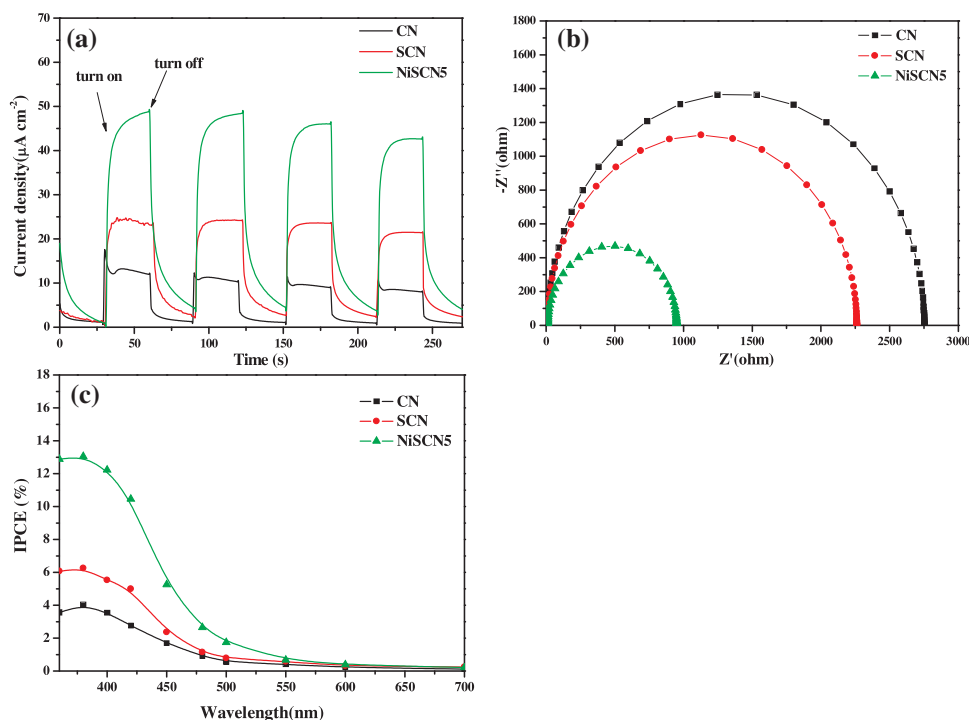


Fig. 10. (a) The transient photocurrent response under visible light irradiation, (b) Electrochemical impedance spectra (EIS) and (c) Incident photon-to-electron conversion efficiency (IPCE) plots of CN, SCN and NiSCN5 samples.

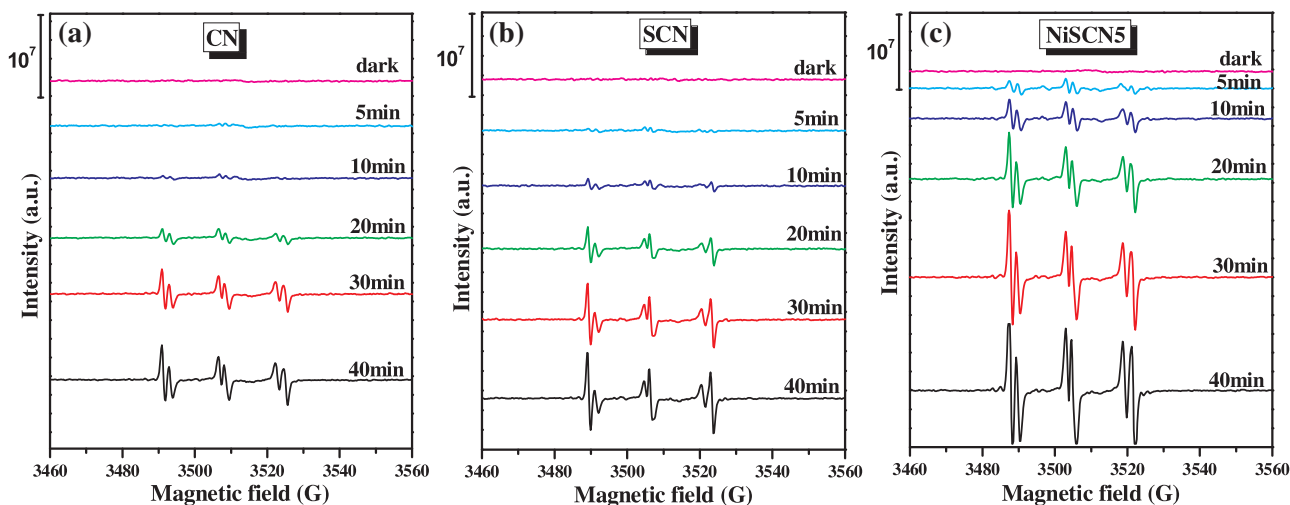


Fig. 11. POBN spin-trapping (POBN-H·) ESR spectra of (a) CN, (b) SCN and (c) NiSCN5.

transfer to Ni nanoparticles due to the excellent electronic conductivity of metal Ni, resulting in the electron-hole separation. The transferred electrons will accumulate on the metal Ni nanoparticles. Then, the  $\text{H}^+$  can easily obtain the electrons on metal Ni to form  $\text{H}\cdot$  radical and then  $\text{H}_2$  forms finally. Meanwhile, large number of holes generated on the VB of SCN, which could directly oxidize the TEOA.

#### 4. Conclusions

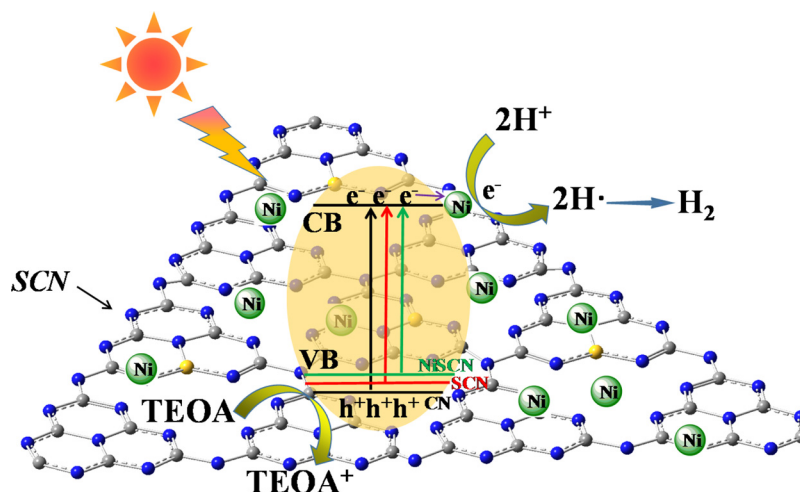
In summary, a series of NiSCN composites were synthesized using a facile method. The NiSCN5 exhibited the best photocatalytic activity of  $\text{H}_2$  evolution from water under visible light irradiation, which was about 334.1 and 83.7 times higher than those of CN and SCN, respectively. According to the experimental and computational results, the good utilization of visible light is responsible for the S and Ni doping, which upshifts the VB potential of CN and narrows the band gap of

photocatalyst. Thus, the nickel species are not only loaded on the surface of SCN, but also doped into the SCN lattice. The significant enhancement on photocatalytic performance is attributed to rapid electron transfer rate and charge separation efficiency induced by surface metal Ni. For the  $\text{H}_2$  evolution reaction, the  $\text{H}^+$  in water can easily obtain the electrons on metal Ni to form  $\text{H}\cdot$  radical and  $\text{H}_2$  forms finally. Our work can provide important enlightenment for understanding and developing of non-noble metal photocatalytic materials.

#### Acknowledgements

This work was supported by the National Natural Science Foundation of China (21403134, 21407060, and 21677069), Shandong Province Development Program of Science and Technology (2014GGX102019), and Jinan Program of Science and Technology (201401240).





**Scheme 1.** The mechanism of the photocatalytic  $\text{H}_2$  production over NiSCN5 under visible light irradiation.

## Appendix A. Supplementary data

Supplementary material related to this article can be found, in the online version, at doi:<https://doi.org/10.1016/j.apcatb.2018.04.050>.

## References

- [1] F. Sordello, C. Minero, *Appl. Catal. B: Environ.* 163 (2015) 452–458.
- [2] G. Bi, J. Wen, X. Li, W. Liu, J. Xie, Y. Fang, W. Zhang, *RSC Adv.* 6 (2016) 31497–31506.
- [3] H. Yu, X. Huang, P. Wang, J. Yu, *J. Phys. Chem. C* 120 (2016) 3722–3730.
- [4] Q. Xiang, B. Cheng, J. Yu, *Angew. Chem. Int. Ed.* 54 (2015) 11350–11366.
- [5] T.F. Jaramillo, K.P. Jørgensen, J. Bonde, J.H. Nielsen, S. Hørch, I. Chorkendorff, *Science* 317 (2007) 100–102.
- [6] A. Fujishima, K. Honda, *Nature* 238 (1972) 37–38.
- [7] J. Liu, Y. Liu, N. Liu, Y. Han, X. Zhang, H. Huang, Y. Lifshitz, S.T. Lee, J. Zhong, Z. Kang, *Science* 347 (2015) 970–974.
- [8] X. Chen, L. Liu, F. Huang, *Chem. Soc. Rev.* 44 (2015) 1861–1885.
- [9] X. Wang, K. Maeda, A. Thomas, K. Takanabe, G. Xin, J.M. Carlsson, K. Domen, M. Antonietti, *Nat. Mater.* 8 (2008) 76–80.
- [10] J. Hu, W. Cheng, S. Huang, D. Wu, Z. Xie, *Appl. Phys. Lett.* 89 (2006) 841–853.
- [11] W. Zhao, G. Yang, S. Wang, H. He, C. Sun, S. Yang, *Appl. Catal. B: Environ.* 165 (2015) 335–343.
- [12] Y. Zhang, T. Mori, J. Ye, M. Antonietti, *J. Am. Chem. Soc.* 132 (2010) 6294–6295.
- [13] X. Chen, J. Zhang, X. Fu, M. Antonietti, X. Wang, *J. Am. Chem. Soc.* 131 (2009) 11658–11659.
- [14] G. Zhang, M. Zhang, X. Ye, X. Qiu, S. Lin, X. Wang, *Adv. Mater.* 26 (2014) 805–809.
- [15] H. Liu, D. Chen, Z. Wang, H. Jing, R. Zhang, *Appl. Catal. B: Environ.* 203 (2017) 300–313.
- [16] L. Ge, C. Han, *Appl. Catal. B: Environ.* 117–118 (2012) 268–274.
- [17] S. Cao, Q. Huang, B. Zhu, J. Yu, *J. Power Sources* 351 (2017) 151–159.
- [18] J. Jiang, S. Cao, C. Hu, C. Chen, *Chin. J. Catal.* 38 (2017) 1981–1989.
- [19] G. Liu, P. Niu, C. Sun, S.C. Smith, Z. Chen, G.Q. Lu, H.M. Cheng, *J. Am. Chem. Soc.* 132 (2010) 11642–11648.
- [20] L. Ke, P. Li, X. Wu, S. Jiang, M. Luo, Y. Liu, Z. Le, C. Sun, S. Song, *Appl. Catal. B: Environ.* 205 (2017) 319–326.
- [21] J. Yang, D. Wang, H. Han, C. Li, *Acc. Chem. Res.* 46 (2013) 1900–1909.
- [22] Y. Shiraishi, Y. Kofuji, S. Kanazawa, H. Sakamoto, S. Ichikawa, S. Tanaka, T. Hirai, *Chem. Commun.* 50 (2014) 15255–15258.
- [23] S. Samanta, S. Martha, K. Parida, *ChemCatChem* 6 (2014) 1453–1462.
- [24] Y. Bu, Z. Chen, W. Li, *Appl. Catal. B: Environ.* 144 (2014) 622–630.
- [25] S. Cao, Y. Li, B. Zhu, M. Jaroniec, J. Yu, *J. Catal.* 349 (2017) 208–217.
- [26] J. Yu, S. Wang, B. Cheng, Z. Lin, F. Huang, *Catal. Sci. Technol.* 3 (2013) 1782–1789.
- [27] J. Yuan, J. Wen, Y. Zhong, X. Li, Y. Fang, S. Zhang, W. Liu, *J. Mater. Chem. A* 3 (2015) 18244–18255.
- [28] S.W. Cao, Y.P. Yuan, J. Barber, S.C.J. Loo, C. Xue, *Appl. Surf. Sci.* 319 (2014) 344–349.
- [29] H. Zhao, S. Sun, P. Jiang, Z.J. Xu, *Chem. Eng. J.* 315 (2017) 296–303.
- [30] J. Dong, M. Wang, X. Li, L. Chen, Y. He, L. Sun, *ChemSusChem* 5 (2012) 2133–2138.
- [31] L. Kong, Y. Dong, P. Jiang, G. Wang, H. Zhang, N. Zhao, *J. Mater. Chem. A* 4 (2016) 9998–10007.
- [32] Y. Wang, X. Wang, M. Antonietti, *Angew. Chem. Int. Ed.* 51 (2012) 68–89.
- [33] X. Bai, L. Wang, Y. Wang, W. Yao, Y. Zhu, *Appl. Catal. B: Environ.* 152–153 (2014) 262–270.
- [34] M. Thommes, K. Kaneko, A.V. Neimark, J.P. Olivier, F. Rodriguez-Reinoso, J. Rouquerol, K.S.W. Sing, *Pure Appl. Chem.* 87 (2015) 1051–1069.
- [35] X. Li, H. Li, S. Huo, Z. Li, *Kinet. Catal.* 51 (2010) 754–761.
- [36] O. Metin, V. Mazumder, S. Ozkar, S. Sun, *J. Am. Chem. Soc.* 132 (2010) 1468–1469.
- [37] J.R. Holst, E.G. Gillan, *J. Am. Chem. Soc.* 130 (2008) 7373–7379.
- [38] S.C. Yan, Z.S. Li, Z.G. Zou, *Langmuir* 25 (2009) 10397–10401.
- [39] X. Rong, F. Qiu, Q. Jiao, Y. Jie, Z. Hao, D. Yang, *J. Ind. Eng. Chem.* 20 (2014) 3808–3814.
- [40] X. Xu, G. Liu, C. Randorn, J.T.S. Irvine, *Int. J. Hydrogen Energy* 36 (2011) 13501–13507.
- [41] J. Yu, K. Wang, W. Xiao, B. Cheng, *Phys. Chem. Chem. Phys.* 16 (2014) 11492–11501.
- [42] J. Wen, X. Li, H. Li, S. Ma, K. He, Y. Xu, Y. Fang, W. Liu, Q. Gao, *Appl. Surf. Sci.* 358 (2015) 204–212.
- [43] B. Zhu, P. Xia, W. Ho, J. Yu, *Appl. Surf. Sci.* 344 (2015) 188–195.
- [44] L. Jiang, X. Yuan, G. Zeng, X. Chen, Z. Wu, J. Liang, J. Zhang, H. Wang, *ACS Sustain. Chem. Eng.* 5 (2017) 5831–5841.
- [45] Q. Fan, J. Liu, Y. Yu, S. Zuo, B. Li, *Appl. Surf. Sci.* 391 (2017) 360–368.
- [46] L. Ge, C. Han, X. Xiao, L. Guo, Y. Li, *Mater. Res. Bull.* 48 (2013) 3919–3925.
- [47] J. Hong, X. Xia, Y. Wang, R. Xu, *J. Mater. Chem.* 22 (2012) 15006–15012.
- [48] E.M. Rockafellow, L.K. Stewart, W.S. Jenks, *Appl. Catal. B: Environ.* 91 (2009) 554–562.
- [49] C. Han, M. Pelaez, V. Likodimos, A.G. Kontos, P. Falaras, K. O'Shea, D.D. Dionysiou, *Appl. Catal. B: Environ.* 107 (2011) 77–87.
- [50] K. Lian, S.J. Thorpe, D.W. Kirk, *Electrochimica Acta* 37 (1992) 2029–2041.
- [51] X. Yan, L. Tian, X. Chen, *J. Power Sources* 300 (2015) 336–343.
- [52] L. Kong, Y. Dong, P. Jiang, G. Wang, H. Zhang, N. Zhao, *J. Mater. Chem. A* 4 (2016) 9998–10007.
- [53] K. Wang, Q. Li, B. Liu, B. Cheng, W. Ho, J. Yu, *Appl. Catal. B: Environ.* 176–177 (2015) 44–52.
- [54] H. Liu, S. Cheng, M. Wu, H. Wu, J. Zhang, W. Li, C. Cao, *J. Phys. Chem. A* 104 (2000) 7016–7020.
- [55] Y. Lv, Y. Liu, Y. Zhu, *J. Mater. Chem. A* 2 (2014) 1174–1182.
- [56] B. Hu, F. Cai, T. Chen, M. Fan, C. Song, X. Yan, W. Shi, *ACS Appl. Mater. Interfaces* 7 (2015) 18247–18256.
- [57] G. Wang, H. Wang, Y. Ling, Y. Tang, X. Yang, R.C. Fitzmorris, C. Wang, J.Z. Zhang, Y. Li, *Nano Lett.* 11 (2012) 3026–3033.
- [58] X. Shi, J. Zhang, G. Cui, N. Deng, W. Wang, Q. Wang, B. Tang, *Nano Res.* 11 (2018) 979–987.